Optical cavities and quantum emitters

Koks, C.

5

OBSERVATION OF MICROCAVITY FINE STRUCTURE

We experimentally show that resonance spectra of optical microcavities have a fine structure that resembles the one observed in atoms. We can identify the polarization-resolved modes in the spectrum and distinguish between two intrinsic effects that cause fine structure: (i) an optical spin-orbit coupling and (ii) nonparaxial propagation and reflection. The measured effects are intrinsic to cavities and are therefore present in any cavity, in contrast to accidental effects like astigmatism. The analogy of fine structure with atomic physics is surprisingly fruitful and gives accurate theoretical predictions which agree with experiments. This analogy can even predict further splittings like a hyperfine splitting, which in our microcavities is explained by a Bragg effect.

C. Koks, F. B. Baalbergen, and M. P. van Exter, Phys. Rev. A 105, 063502 (2022)

5.1. INTRODUCTION

The fine structure in atomic spectra has revealed perturbations to the Hamiltonian which are intrinsic for atoms [108]. The Bohr model in atomic physics predicts groups of degenerate orbitals, labeled by the principal quantum number n. This degeneracy is lifted by perturbations such as spin-orbit coupling and a relativistic correction [109]. We observe a spectral fine structure in optical microcavities which reveals similar intrinsic perturbations to the paraxial wave equation. The paraxial model predicts groups of frequency-degenerate transverse modes, labeled by the transverse order N [33]. Also their degeneracy is lifted by perturbations which are intrinsic to microcavities. This analogy gives accurate predictions [110] that agree with the experiments presented in this chapter.

The microcavity fine structure becomes relevant when the radius of curvature of the mirror R is small. More specifically, the fine structure is proportional to λ/R and typically observable when $F\lambda/R > 10$, where F is the cavity finesse [33]. These intrinsic corrections are always present in optical cavities and dominate over external, mirror-shape-dependent effects, such as astigmatism, when λ/R is large enough.

The frequency splittings that have been reported in literature are typically for cavities with relatively large radii of curvature, $R \gg \lambda$, where the intrinsic effects are small and the external effects of astigmatism [31, 32, 68, 99] and birefringence [111] dominate. Intrinsic effects of fine structure have been reported for microwave cavities [69, 73] where λ is large, but its eigenmodes were not observed. In the optical domain, only some aspects of the fine structure have been reported in a conference proceeding [90]. We are the first to measure the complete fine structure and its eigenmodes. We use close to perfect

rotational-symmetric microcavities with very small radii of curvature, where the intrinsic effects are most clearly distinguishable.

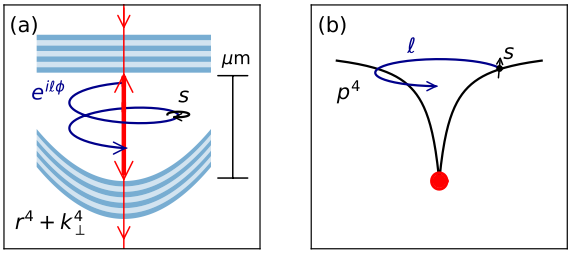

Figure 5.1: Analogy between optical microcavity and atom. (a) Optical field with spiral wavefront $e^{il\phi}$ and circular polarization s between a flat and curved mirror. (b) Electron wavefunction with orbital angular momentum ℓ and electron spin s.

5

This chapter shows how the intrinsic effects of spin-orbit coupling and nonparaxial propagation and reflection determine the fine structure. In the experiment, the cavity length is scanned to obtain resonance spectra of four optical microcavities with radii of curvature between $R = 2.5(5) - 17.3(2)$ μm. The chapter presents the full analysis for the $R = 5.8(2)$ μm cavity and briefly discusses the results from other cavities. The resonant modes in the spectrum are first labeled with transverse order N, according to paraxial theory. A fine structure is observed by zooming in on each N group. Every mode in the fine structure is further identified using a polarization-resolved CCD camera. The fine structure is studied systematically and compared to theory. A third type of splitting is reported, which we call "hyperfine splitting" and which is dominantly due to a Bragg effect [100].

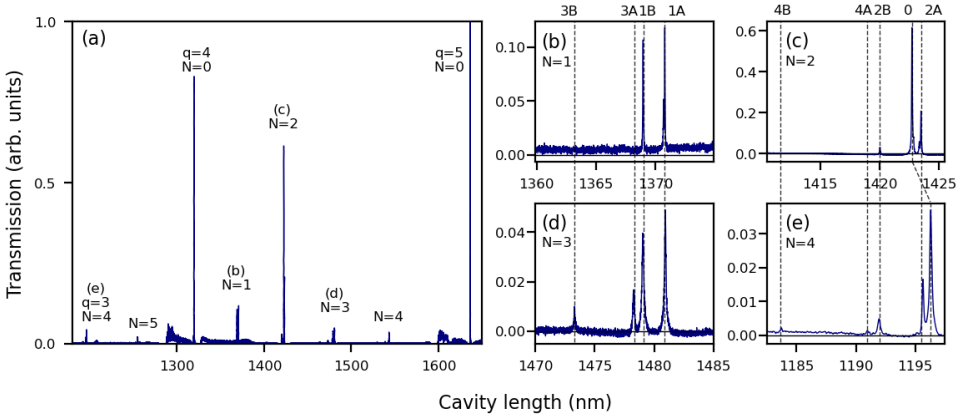

Figure 5.2: Cavity transmission spectrum shows fundamental and higher-order transverse modes. (a) Transmission versus cavity length as a function of the cavity length, where q, N indicate the longitudinal and transverse mode number. (b-e) Zoom-ins of the groups N=1 to N=4 show fine structure. The broad peaks around $L = 1300$ nm and $L = 1600$ nm are resonances of planar modes formed next to the microcavity.

The analogy of microcavity fine structure to that of atoms is surprisingly fruitful and

gives new predictions [110] that agree with experiments. Figure 5.1 illustrates the perturbations in both systems. In atoms, spin-orbit coupling couples the orbital angular momentum ℓ and the spin s of an electron through the magnetic field. In microcavities, spin-orbit coupling couples the angular momentum ℓ and circular polarization spin s of light [98, 112]. The optical spin-orbit coupling originates from a projection of the longitudinal component of the electric field [85] into an additional small transverse component at the mirror surface. The relativistic correction in atoms is a quartic p^4 correction to the momentum, which shifts all modes proportional to ℓ^2. As a direct analogy, a nonparaxial momentum correction $k_\perp^4$ is required for microcavities with large opening angles [69, 81], which also shifts all modes proportional to ℓ^2. In addition, the nonparaxial theory contains a r^4 correction from higher-order Taylor expansions of the mirror and wavefront shape [60].

5.2. LABELING OF CAVITY EIGENMODES

Paraxial theory predicts resonant cavity lengths that only depend on the longitudinal mode number q, transverse order N, and Gouy phase $\chi = \arcsin\sqrt{(L+2L_\mathrm{D})/R}$, where L_D is the modal DBR penetration depth [53]. We experimentally determine the radius of curvature from the transverse mode spacings between each N group, which are equidistant in the paraxial theory [53]. A more complete (nonparaxial) description from [110] contains the fine structure splittings $\Delta\tilde{L}$,

$$L = \frac{\lambda}{2}\left[q + \frac{N+1}{\pi}\chi + \Delta\tilde{L}\right], \tag{5.1}$$

where

$$\Delta\tilde{L} = \frac{1}{2\pi kR}\left[-\ell\cdot s - \left(\frac{3}{8} - \tilde{p}\frac{L}{8(R-L)}\right)\ell^2 + f(N)\right]. \tag{5.2}$$

This equation includes the two corrections: (i) the spin-orbit coupling, scaling with $l\cdot s$, and (ii) the quartic corrections $k_\perp^4$ and r^4, scaling with ℓ^2. The quartic corrections shift the modes by a factor $3\ell^2/8$ when using a perfectly spherical mirror. Perturbations to this mirror shape are quantified by the aspheric correction $\tilde{p}$ defined as $z_\mathrm{mirror} - z_\mathrm{sphere} = -\tilde{p}\frac{r^4}{8R^3}$. The term $f(N)$ shifts all modes of transverse order N by the same amount and goes unnoticed in the fine structure.

Our planar and curved Distributed Bragg Reflectors (DBR) are produced by Oxford HighQ [59] and have a reflectivity of 99.9 % (finesse $F \approx 3000$). The curved mirror is illuminated with a HeNe laser ($\lambda = 633$ nm). The cavity length is scanned with piezo-stacks and the light is transmitted through the microcavity at resonant cavity lengths. This transmitted light is detected with a photodiode and a polarization-resolving CCD camera.

Figure 5.2a shows a typical microcavity transmission spectrum, for the $R = 5.8(2)$ μm cavity. The peaks are located at resonant cavity lengths L. We can label them with q and N according to paraxial theory, which predicts that each transverse group N consists of $2(N+1)$ orthogonal modes. Figures 5.2b-e zoom in on each N group. This shows that, in practice, each group typically consists of $N+1$ modes. The dashed lines suggest that all odd (or even) N-groups have similar mode and fine structures, albeit that larger N-groups contain more modes. The 0-mode for the even N groups is shifted due to the shape of the mirror (see below).

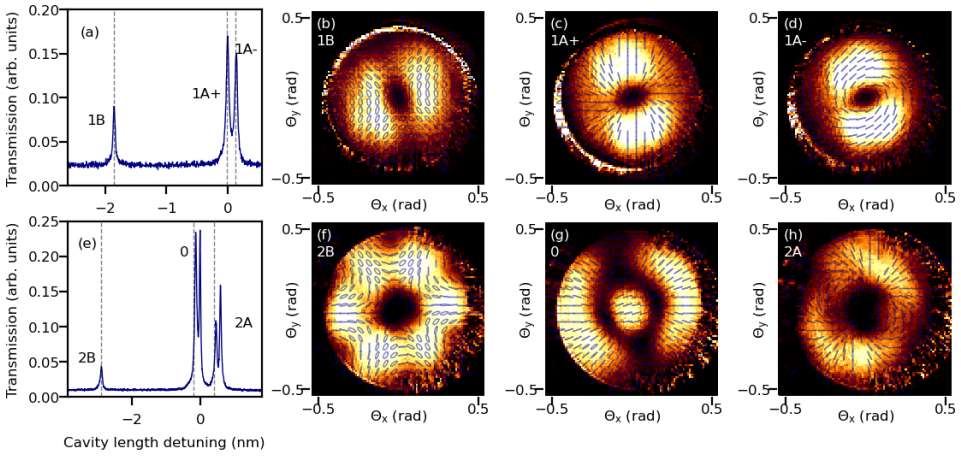

Figure 5.3: Fine structure splittings of the (a-d) N=1 and (e-h) N=2 transverse mode groups. The dashed lines in (a) and (e) correspond to polarization resolved CCD images (b-d) and (f-h), where the order from left to right corresponds to a smaller to larger cavity length detuning in (a) and (e). Each ellipse shows the local direction and circularity of the polarization.

5

Figure 5.3 shows the spectrum and CCD images of the polarized eigenmodes of the $N = 1$ and $N = 2$ groups. The eigenmodes of the $N = 3$ and $N = 4$ groups are shown below in Fig. 5.5. The mode labels ℓA and ℓB ($\ell > 0$) in Fig. 5.2 and 5.3 are identified from the CCD images as follows. The angular momentum ℓ is determined by inspecting the intensity profile and comparing it to the scalar Laguerre-Gaussian modes [33]. For instance, the $N = 2$ modes in Figs. 5.3f and 5.3h have a dark center and one ring, corresponding to $\ell = 2$, whereas Fig. 5.3g has a bright center, corresponding to $\ell = 0$. The A/B labels are determined from the polarization patterns, where the pattern of the A/B modes resemble circular/hyperbolic flow lines. The total angular momentum $j = l + s$ ($s = -1$ for A and $s = 1$ for B modes) is visible in the rotation symmetry of the polarization pattern, which remains unchanged after rotation over an angle π/j (rotational symmetric at $j = 0$).

Each of the $N+1$ modes is typically two-fold degenerate, because of its polarization degrees of freedom. This degeneracy can be lifted under certain conditions. Figure 5.3a shows this so-called "hyperfine" splitting for mode $1A$. The modes are labeled $+/-$ and have orthogonal polarization patterns. The CCD images of the modes $1A-$ and $1A+$, shown in Figs. 5.3c and d, show that their polarization is in the azimuthal and radial direction, respectively. Figure 5.3e also shows a hyperfine splitting for the 0 and $2A$ modes. Fig. 5.3g and 5.3h show the modes with the mostly radial polarization direction, which correspond to the left peaks in the hyperfine splitting of the 0 and the $2A$ modes in Fig. 5.3e.

Figure 5.4 shows the measured spin-orbit splitting ΔL_{SO} between the ℓA and ℓB modes. The green points correspond to the $R = 5.8(2)$ μm cavity presented in Figs. 5.2 and 5.3, while the other points are measured for three other cavities. All spin-orbit splittings scale linearly with the angular momentum ℓ.

5.3. COMPARISON WITH THEORETICAL PREDICTIONS

Figure 5.4 also shows the theoretical prediction of spin-orbit coupling ΔL_{SO} based on the measured radius of curvature R. The figure shows that the measured splittings follow the theory well for all four cavities, showing that spin-orbit coupling in these cavities dominates over external perturbations. It also shows the inverse proportionality with R of the fine structure splittings.

Theory predicts that a quartic perturbation shifts both ℓA and ℓB modes by the same amount, such that their resonant cavity lengths decrease proportional to ℓ^2. The data in figure 5.2 agrees reasonably well with this prediction. To quantify this effect, we look at the average position of the ℓA and ℓB modes, given by $\ell\overline{AB}$, and compare it with $(\ell+2)\overline{AB}$. From equation 5.2 we find that such splittings are $\Delta L_{\text{quartic,th}}/(\lambda/2) = 3(\ell+1)/(4\pi kR)$. Theory predicts for $N = \ell+2 = 2,3,4$ that $\Delta L_{\text{quartic,th}} = 1.31(5)$ nm, 2.62(9) nm and 3.9(1) nm. The measured splittings are $\Delta L_{\text{quartic}} = 0.93(5)$ nm, 4.17(7) nm and 6.3(1) nm. The measured values have the same sign and order of magnitude as the theoretical values but differ because of an aspheric correction $\tilde{p}\frac{L}{8(R-L)} = 0.11(1)$, $-0.20(1)$, and $-0.23(1)$. The decreasing value for $\tilde{p}$ suggests that the cavity is flatter for compact (low N) modes and steeper for larger (high N) modes. This agrees with the "bathtub" shape which was observed in AFM measurements [94].

The hyperfine splitting of the $1A$ modes in Fig 5.3a can be explained by the Bragg effect. It occurs because the DBRs have an angle-dependent penetration depth, which is opposite for radial ($1A+$) and azimuthal ($1A-$) polarized light [55, 100]. The measured distance of 0.12(2) nm between the $1A+$ and $1A-$ modes can be explained by a small wavelength detuning from the stopband center of the DBR. The hyperfine splitting of 0.15(2) nm of the 0 and $2A$ modes in Fig. 5.3a can also be explained by the Bragg effect. The 0 and $2A$ modes mix due to astigmatism, such that the mode profiles become more radially and azimuthally polarized. The mixing ratio of the 0 and $2A$ modes is almost the same, which explains why the hyperfine splitting is also almost the same (see Appendix 5.B).

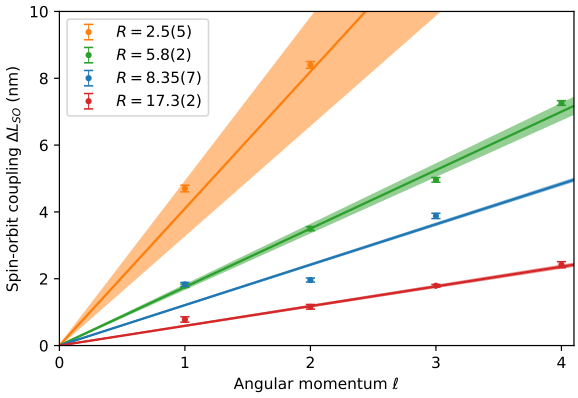

Figure 5.4: Observed mode splitting due to spin-orbit coupling for four different cavities. The lines show the theoretically predicted value with uncertainty for each radius of curvature.

5.4. ASTIGMATIC CORRECTION

The fine structure is modified when the mirror shape is non-ideal i.e., does not have a perfect spherical shape. Up to first order in the Taylor expansion, this non-ideal mirror shape can be described with two dimensionless parameters: $\tilde{p}$ for the aspheric correction and X for the astigmatic correction. In this section we investigate the influence of astigmatism on the fine structure.

We model the combined effect of both the astigmatic and aspheric corrections with a $(N+1)\times(N+1)$ coupling matrix. The diagonal elements of this matrix are given by Eq. (5.2). The off-diagonal elements contain the relative astigmatism X, defined as $X = 4kR\eta_{astig}\tan(\chi)$ with $\eta_{astig} = (R_{max} - R_{min})/(2R)$, where R_{max} and R_{min} are the radii of curvature along the long and short axes of the mirror and $R = (R_{max} + R_{min})/2$. This dimensionless parameter X is unity when the astigmatic and intrinsic effects on the fine structure are approximately equally strong. If X is small, $|X| < 1$, the matrix is close to diagonal, and the eigenmodes are like lA/B modes. On the other hand, if X is large, $|X| \gg 1$, the off-diagonal elements are large and the lA/B modes strongly couple to each other. The newly formed eigenmodes then obtain a strong Hermite-Gaussian character, as one would expect for a cavity with large astigmatism. More aspects of this model are described in ref. [110] The explicit model for the $N = 4$ group is shown in appendix 5.A.

Figure 5.5 shows the polarization resolved CCD images of the $N = 3$ and $N = 4$ modes for the $R = 5.8(2)$ μm cavity. The 0 and $2A$ modes in Figs. 5.5k and 5.5l show a clear astigmatic coupling. The other modes are more difficult to identify, because some modes have an opening angle larger than the numerical aperture of the imaging lens ($NA = 0.5$), like in Figs. 5.5b and 5.5h, or are mixed with planar modes causing a bright center, like in Figs. 5.5b-d and and 5.5h-j. However, these modes seem relatively uninfluenced by the astigmatic correction.

The observed fine structure spectrum of the $N = 4$ mode is used to find the parameters $\tilde{p}$ and X. Figs. 5.6a and 5.6b show the calculated eigenvalues and its corresponding eigenmodes. The horizontal dashed lines show the measured eigenvalue, to which the model is fitted. This fit yields an aspheric correction $\tilde{p}\frac{L}{8(R-L)} = -0.22(2)$ and relative astigmatism $X = 0.7(2)$, which corresponds to an absolute astigmatism of $\eta_{astig} = 0.6(2)$ %. Note that the fitted value of $\tilde{p}\frac{L}{8(R-L)} = -0.22(2)$, obtained from the full spectrum with astigmatism, is in close agreement with the value $\tilde{p}\frac{L}{8(R-L)} = -0.23(1)$ found in Sec. 5.3, from only the $2A/B$ and $4A/B$ modes and only considering the aspheric correction. Also the calculated eigenmodes in Figs. 5.6c-g correspond well to the measured eigenmodes in Figs. 5.5h-l. From the calculated eigenmodes, we also find that the mode in 5.5k is "mostly 2A" and the mode in 5.5l is "mostly 0", meaning that the eigenmodes are dominated by 0 and $2A$ modes (see appendix 5.B).

5.5. CONCLUSION

In conclusion, we have observed fine structures in the resonance spectra of microcavities. This fine structure is explained by two intrinsic perturbations. First, the spin-orbit coupling causes a frequency splitting between the ℓA and ℓB modes that scales with ℓ. Second, the quartic terms $k_\perp^4$ and r^4 shift both ℓA and ℓB by the same amount that scales with ℓ^2. A parameter $\tilde{p}$ was introduced to quantify the aspheric shape of the mirror. Furthermore, a hyperfine splitting was observed in the $1A+/1A-$ mode, which could be ex-

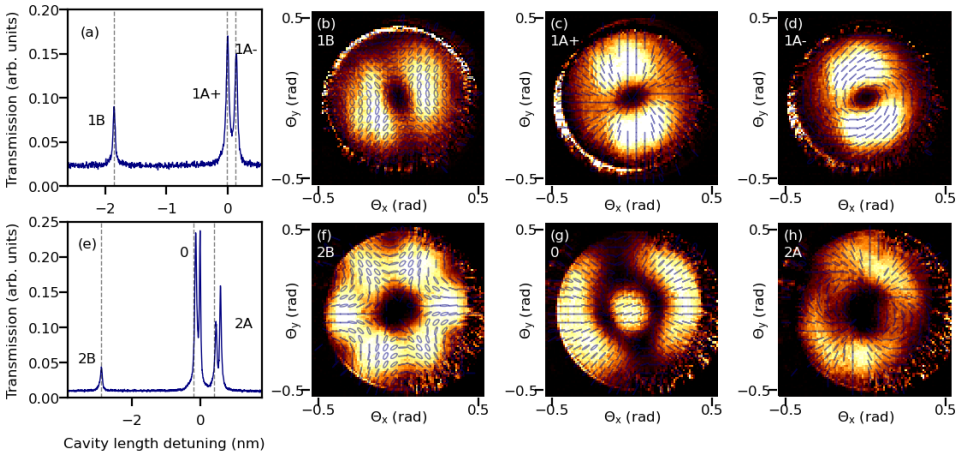

Figure 5.5: Fine structure splittings of the (a-f) N=3 and (g-i) N=4 transverse mode groups. The dashed lines in (a) and (g) correspond to the polarization resolved CCD images (b-f) and (h-l), where the order from left to right corresponds to a smaller to larger cavity length detuning in (a) and (g) and where (e) and (f) are two images of the $1A+$ and $1A-$ mode whose hyperfine splitting is not resolvable in the spectrum in (a). Each ellipse shows the local direction and circularity of the polarization.

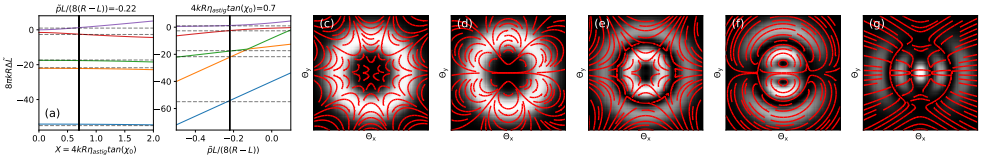

Figure 5.6: Simulation of the combined effects of astigmatic and aspheric corrections on resonance frequencies and mode profiles. (a-b) Frequency shifts as a function of the (a) astigmatic correction X and (b) aspheric correction $\tilde{p}$ around the fitted values (vertical lines) deduced from the measured frequencies (horizontal dashed lines) of the $N = 4$ modes in the $R = 5.8(2)$ μm cavity. (c-g) Mode profiles in order of frequency at the vertical lines in (a-b); mode in (c) has lowest frequency.

plained by the polarization dependence of the penetration depth in the DBR. Measurements on other cavities with different radii of curvature showed that the fine structure splittings scale with λ/R. We used a model to calculate the influence of aspheric and astigmatic corrections on the fine structure and found a modest relative astigmatism $X = 0.7(2)$ ($\eta_{astig} = 0.6(2)\%$), which indicates that the intrinsic effect dominate over the external effects. The analogy with fine structure in atomic physics helps to understand the full spectrum and even some aspects of the hyperfine structure.

As an outlook, we note that the observation and analysis of the (micro)cavity fine structure introduces a new technique that has impact in different areas. First, it can serve as a tool to measure the theoretical predictions for nonparaxial optical vector fields [86, 100, 110]. Second, it can be used for imaging [30], enabling the analysis of mirror shapes with sub-nanometer precision, using shape parameters like $\tilde{p}$, X and higher-order terms [110]. And finally, it affects the efforts to increase light-matter interaction in optical cavities [27, 29]. The strength of light-matter interaction is given by the Purcell factor, which is usually written as the ratio of the quality factor over the mode volume $F_p \sim Q\lambda^3/V$. This can equally be written as the ratio of the Finesse F over the mode area A, $F_p \sim F\lambda^2/A$. As the mode area scales like $A \sim \lambda\sqrt{LR}$ one can also write the Purcell factor as $F_p \sim F\lambda/\sqrt{RL} > F\lambda/R$. Our earlier statement that fine structure effects are typically observable when $F\lambda/R > 10$ means that these effects are unavoidable in open cavities with a large Purcell factor. Moreover, if λ/R is large enough, the intrinsic contributions tend to dominate over external effects and the spin-orbit coupling, quartic term, and Bragg effect are essential to fully describe the microcavity modes.

We would like to thank A. A. P. Trichet from Oxford HighQ for providing us with the mirror samples. We also acknowledge Sean van der Meer and Martin Bijl for supporting experiments, Martijn Wubs for supporting theory and Pepijn Pinkse for stimulating discussions.

5.A. COUPLING MATRIX FOR ASTIGMATIC AND ASPHERIC CORRECTIONS

The fine structure splitting is determined by the eigenvalues of a $(N+1)\times(N+1)$ matrix, with a basis of the lA, lB and 0 eigenmodes. Here, we present the explicit matrix used to calculate the eigenfrequencies and eigenmodes in section 5.4. More details and other coupling matrices can be found in Ref. [110].

For $N = 4$, we choose the basis $(4B, 2B, 0, 2A, 4A)$. The coupling matrix is given by

$$8\pi kR\Delta\tilde{L} = \begin{pmatrix} -40+\frac{8\tilde{p}L}{R-L} & 2X & 0 & 0 & 0 \\ 2X & -14+\frac{2\tilde{p}L}{R-L} & \sqrt{6}X & 0 & 0 \\ 0 & \sqrt{6}X & 0 & \sqrt{6}X & 0 \\ 0 & 0 & \sqrt{6}X & 2+\frac{2\tilde{p}L}{R-L} & 2X \\ 0 & 0 & 0 & 2X & -8+\frac{8\tilde{p}L}{R-L} \end{pmatrix}. \tag{5.3}$$

The diagonal elements contain the rotational symmetric components, being the non-

paraxial perturbations and the aspheric correction. The off-diagonal elements contain the relative astigmatism X. The resonant frequencies $8\pi kR\Delta\tilde{L}$ are found by diagonalizing the matrix. In the case of zero astigmatism, the matrix is already diagonal and its eigenvalues directly follow from Eq. (5.2).

For small values of X, the modes are relatively uncoupled and only modes that are close in frequency are influenced by astigmatic coupling, which is the case for the 0 and $2A$ modes for the $N = 4$ group, corresponding to the third and fourth row and column of the matrix in Eq. (5.3). The mixed modes in Figs. 5.6f and 5.6g can approximately be written as a superposition of the 0 and $2A$ modes, $|\psi\rangle = \alpha|2A\rangle + \beta|0\rangle$, where $|\alpha|^2 + |\beta|^2 = 1$. The calculated parameters are $\alpha = 0.84$ and $\beta = 0.54$ for the mode that is "mostly $2A$" in Fig. 5.6f and $\alpha = -0.54$ and $\beta = 0.84$ for the mode that is "mostly 0" in Fig. 5.6g.

In Sec. 5.3 we noted that $\tilde{p}$ varied with the mode number N. The parameter is $\tilde{p}\frac{L}{8(R-L)} = 0.11$ for the $N = 2$ group, while $\tilde{p}\frac{L}{8(R-L)} = -0.22$ for the $N = 4$ group. This change affects the mixed character of some modes. Figure 5.6b shows an avoided crossing for the 0 and $2A$ modes (red and purple lines) around $\tilde{p}\frac{L}{8(R-L)} \approx -0.1$. In case of the $N = 2$ group, the parameter $\tilde{p}\frac{L}{8(R-L)}$ is on the positive side of the avoided crossing, hence the 0 mode has a smaller eigenfrequency than the $2A$ mode. In case of the $N = 4$ group, the parameter is on the negative side and the 0 mode has a larger eigenfrequency than the $2A$ mode. This switch of the 0 and $2A$ modes is also measured in the spectra of the $N = 2$ and $N = 4$ groups in Fig. 5.2.

5.B. HYPERFINE SPLITTING

A hyperfine splitting of 0.12(2) nm was observed for the $1A$ modes in Fig. 5.3a and a hyperfine splitting of 0.15(2) nm was observed for the 0 and $2A$ modes in Fig. 5.3e. The $1A$ hyperfine splitting was theoretically expected in a rotational symmetric system, but the 0 and $2A$ hyperfine splitting not. The 0 and $2A$ hyperfine splitting indicates that rotational symmetric is broken. In this section, we estimate the contribution of astigmatism to this hyperfine splitting. We consider two mechanisms by which astigmatism can cause hyperfine splitting: (i) the Bragg effect and (ii) shape birefringence. We find that the Bragg effect, in combination with mode mixing, is the dominant cause of hyperfine splitting for the 0 and $2A$ modes.

5.B.1. BRAGG EFFECT

The Bragg effect originates from a difference between the penetration depth of radial and azimuthal polarization. The observed hyperfine splitting of the $1A$ mode shows a clear distinction between the radial polarization for the mode $1A+$ and azimuthal polarization for the mode $1A-$. We observed a hyperfine splitting of 0.12(2) nm for the $1A+$ and $1A-$ modes, which we fully attribute to the Bragg effect.

At first sight, one would expect that other modes are not affected by the Bragg effect, because their polarization patterns contain equal amounts of radial and azimuthal polarization and rotational symmetry averages out the penetration depths. However, astigmatism breaks rotational symmetry, as the mixed eigenmodes for the $N = 2$ group in Figs. 5.3g and 5.3h show. These figures show only one of the "+" or "-" peaks in the hyperfine splitting. Figure 5.7 shows the calculated modes profiles of all the $N = 2$ modes, based

on the parameters $\tilde{p}\frac{L}{8(R-L)} = 0.11$ and $X = 0.7$, with the "+" modes in the top row and the "-" modes in the bottom row. In case of a perfect rotational symmetric cavity, the modes in each column are frequency degenerate. However, the right two columns show differences in their polarization profiles, which causes the hyperfine splitting. Figs. 5.7b and 5.7f show modes which have most intensity in the radial polarization direction and Figs. 5.7c and 5.7e show modes which have most intensity in the azimuthal polarization direction. This modified intensity distribution causes the Bragg effect for the modes other than $1A$.

We will now calculate the hyperfine splitting of these mode relative to the hyperfine splitting of the $1A$ mode of the $N = 1$ group. The modes are written as mixed modes of the form $|\psi_{2A\pm}\rangle = \alpha|2A\rangle \pm \beta|0\rangle$ and $|\psi_{0\pm}\rangle = \alpha'|2A\rangle \pm \beta'|0\rangle$ with $|\alpha|^2 + |\beta|^2 = 1$, $|\alpha'|^2 + |\beta'|^2 = 1$. The $\pm$ correspond to the top and bottom row in Fig. 5.7. We then calculate the perturbation of the Bragg effect H_{Bragg} [110] of the 0 and $2A$ modes, relative to the $1A$ modes: $\langle 0|H_{\text{Bragg}}|2A\rangle = \sqrt{2}\langle 1A|H_{\text{Bragg}}|1A\rangle$ and $\langle 0|H_{\text{Bragg}}|0\rangle = \langle 2A|H_{\text{Bragg}}|2A\rangle = 0$. Thus, the hyperfine splitting of the "mostly 2A" and "mostly 0" modes can be expressed as $\Delta\tilde{\nu}_{\text{theory}} = 2\sqrt{2}\alpha\beta\Delta\tilde{\nu}_{1A}$.

The calculated values of α and β, based on the astigmatism of $\eta_{\text{astig}} = 0.6(2)\%$ and the measured aspheric correction of $\tilde{p}\frac{L}{8(R-L)} = 0.11(1)$ for the $N = 2$ group, are $\alpha = 0.97(2)$ and $\beta = 0.24(6)$ for the mode which is "mostly $2A$" and $\alpha = 0.24(6)$ and $\beta = 0.97(2)$ for the mode which is "mostly 0". The calculated hyperfine splitting for both the "mostly $2A$" and "mostly 0" mode relative to the $1A$ mode is thus $\Delta\tilde{\nu}_{\text{theory}}/\Delta\tilde{\nu}_{1A} = 0.6(2)$. Using the measured hyperfine splitting of 0.12 nm for the $1A+/-$, we thus expect that the hyperfine splitting of the 0 and $2A$ modes is $\Delta L_{\text{theory}} = 0.07(3)$ nm. The measured value of the hyperfine splitting is $\Delta L_{\text{measured}} = 0.15(2)$ nm. The Bragg effect can thus partially explain the hyperfine splitting.

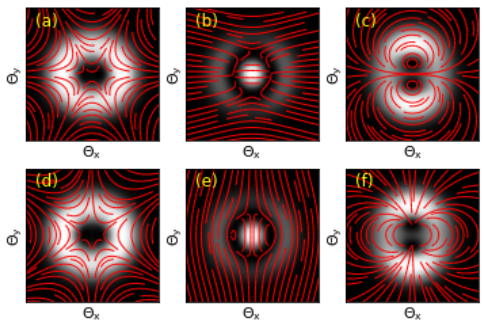

Figure 5.7: Calculated modes of the N=2 group: (a-c) modes of the "+" group, (d-f) modes of the "-" group. From left to right the 2B, 0 and 2A modes in order of increasing resonance frequencies. The red lines indicate the polarization profile.

5.B.2. SHAPE BIREFRINGENCE

The ellipsoidal mirror shape can also cause birefringence between modes polarized along the long and short axes. This effect is a perturbation on the spin-orbit coupling, where the transverse field components in the cavity are projected on the curved mirror, but by

a different amount for the two axes of the ellipsoid [110]. This shape birefringence was observed before in the hyperfine splitting of the fundamental mode ($N = 0$) [30, 99]. The effect on modes with $\ell \neq 0$ is more subtle, and the proper perturbation that contributes to this effect is see also [110]

$$H_{SB} = \frac{\eta_{astig}}{\pi kR}(\hat{x}x - \hat{y}y)(\partial_x \hat{x} + \partial_y \hat{y}). \tag{5.4}$$

Calculating the coupling between the + and − modes gives

$$\Delta\nu_{SB} = 2\alpha\beta\langle 0\pm|\frac{H_{SB}}{2\pi}|2A\pm\rangle = \mp 2\alpha\beta\frac{\eta_{astig}}{4\pi kR}. \tag{5.5}$$

For $\eta_{astig} = 0.6(2)\%$ and $\tilde{p}\frac{L}{8(R-L)} = 0.11(1)$, the calculated hyperfine splitting is 0.0012(6) nm and therefore we can safely neglect it. Hence, we conclude that the hyperfine splitting for the $R = 5.8(2)$ μm cavity is caused by the combined action of astigmatism and a Bragg effect and that shape birefringence plays a negligible role.

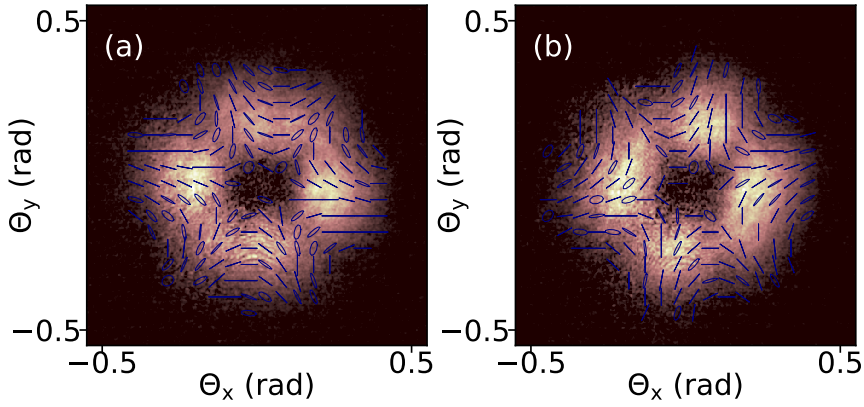

Figure 5.8: Measured 2B modes for the N=2 group in a $R = 17.1$ μm cavity: (a) 2B+ mode, (b) 2B- mode. Each ellipse shows the local direction and circularity of the polarization.

5.B.3. LARGE ASTIGMATISM

The effect of shape birefringence can become more important in case of large astigmatism. Fig. 5.8 shows the $2B$ modes for a different $R = 17.1(2)$ μm cavity with a large relative astigmatism $X \approx 14$, which corresponds to $\eta_{astig} \approx 5$ %. For this cavity, we observed a hyperfine splitting of 0.22(3) nm between the $2B+$ and $2B-$ modes. The polarization profiles of the eigenmodes show that most intensity is in the horizontal polarization direction for the mode $2B+$ in Fig. 5.8a and in the vertical polarization direction for the mode $2B-$ in Fig. 5.8b. The Bragg effect should average out, since the modes contain equal amounts of radial as azimuthal polarization. The shape birefringence is a more plausible cause for the observed splitting since this acts on the horizontal or vertical polarization.